Research article

Francesco Todisco*, Radu Malureanu, Christian Wolff, P. A. D. Gonçalves, Alexander S. Roberts, N. Asger Mortensen* and Christos Tserkezis*

Magnetic and electric Mie-exciton polaritons in silicon nanodisks

https://doi.org/10.1515/nanoph-2019-0444
Received October 25, 2019; revised December 17, 2019; accepted February 4, 2020

Abstract: Light-matter interactions at the nanoscale constitute a fundamental ingredient for engineering applications in nanophotonics and quantum optics. In this regard, Mie resonances supported by high-refractive index dielectric nanoparticles have recently attracted interest, due to their lower losses and better control over the scattering patterns compared to their plasmonic counterparts. The emergence of several resonances in high-refractive index dielectric nanoparticles results in an overall high complexity, where the electric and magnetic dipoles can show a significant spectral overlap, especially at optical frequencies, thus hindering possible light-matter coupling mechanisms arising in the optical spectrum. This behavior can be properly adjusted by using non-spherical geometries, an approach that has already been successfully exploited to tune directional scattering from dielectric nanoresonators. Here, by using cylindrical nanoparticles, we show, experimentally and theoretically, the emergence of peak splitting for both magnetic and electric dipole resonances of individual silicon nanodisks coupled to a J-aggregated organic semiconductor. In the two cases, we find that the different character of the involved resonances leads to different light-matter coupling regimes. Crucially, our results show that the observed energy splittings are of the same order of magnitude as the ones reported using similar plasmonic systems, thereby confirming dielectric nanoparticles as promising alternatives for localized strong coupling studies. The coupling of both the electric and magnetic dipole resonances can offer interesting possibilities for the control of directional light scattering in the strong coupling regime and the dynamic tuning of nanoscale light-matter hybrid states by external fields.

Keywords: Mie resonances; silicon nanoparticles; strong coupling; magnetic dipole; electric dipole; resonance splitting; polaritons.

***Corresponding authors: Francesco Todisco and Christos Tserkezis,** Center for Nano Optics, University of Southern Denmark, Campusvej 55, DK-5230 Odense M, Denmark, e-mail: francesco.todisco@nanotec.cnr.it (F. Todisco); ct@mci.sdu.dk (C. Tserkezis). https://orcid.org/0000-0002-0188-6048 (F. Todisco); https://orcid.org/0000-0002-2075-9036 (C. Tserkezis); and **N. Asger Mortensen,** Center for Nano Optics, University of Southern Denmark, Campusvej 55, DK-5230 Odense M, Denmark; Center for Nanostructured Graphene, Technical University of Denmark, DK-2800 Kongens Lyngby, Denmark; and Danish Institute for Advanced Study, University of Southern Denmark, Campusvej 55, DK-5230 Odense M, Denmark, e-mail: asger@mailaps.org. https://orcid.org/0000-0001-7936-6264
Radu Malureanu: Department of Photonic Engineering, Technical University of Denmark, DK-2800 Kongens Lyngby, Denmark
Christian Wolff and Alexander S. Roberts: Center for Nano Optics, University of Southern Denmark, Campusvej 55, DK-5230 Odense M, Denmark. https://orcid.org/0000-0002-5759-6779 (C. Wolff)
P. A. D. Gonçalves: Center for Nano Optics, University of Southern Denmark, Campusvej 55, DK-5230 Odense M, Denmark; Department of Photonic Engineering, Technical University of Denmark, DK-2800 Kongens Lyngby, Denmark; and Center for Nanostructured Graphene, Technical University of Denmark, DK-2800 Kongens Lyngby, Denmark. https://orcid.org/0000-0001-8518-3886

1 Introduction

Light-matter interactions constitute a fundamental field of study in photonics, since it opens routes for exploring novel physical phenomena and for exploiting applications in optoelectronics and quantum optics [1]. Although the field started growing around high quality-factor cavities with extremely low losses and diffraction-limited mode volumes [2, 3], in recent years increasing interest has been devoted to pushing the research down to the nanoscale by using open nanocavities, with the promise of shrinking light-matter interaction lengths down to scales much smaller than a single wavelength [4] and manipulating the generation of nonclassical light by quantum emitters [5].

In this regard, plasmonic resonances localized in metallic nanoparticles have so far been the preferential studied platform [6]. Indeed, their ability to enhance and

Open Access. © 2020 Francesco Todisco, N. Asger Mortensen, Christos Tserkezis et al., published by De Gruyter. This work is licensed under the Creative Commons Attribution 4.0 Public License.

concentrate light in extremely sub-wavelength volumes, together with their high sensitivity to the environment's refractive index, makes them ideal platforms to study the interactions with nearby molecules or quantum emitters. As a result, exciting effects have been observed so far, including Purcell enhancement [7, 8], enhanced Raman [9] and fluorescence [10, 11] spectroscopy, localized heating [12] and sensing [13, 14].

Of particular interest is the case when light-matter interactions enter the so-called strong coupling regime. This happens when the coupling strength exceeds the overall system losses, meaning that (nano)cavity photons and nearby emitters can coherently exchange energy, while the emitter occupation oscillates at the so-called Rabi frequency [1]. Consequently, the system becomes an effective mixture of light and matter components, dubbed as polaritons, characterized by a peak splitting in the scattering and absorption spectra and by the emergence of an anti-crossing in the dispersion. Furthermore, as effective light-matter mixtures, polaritons offer the unique potential of dressing photons with nonlinearities [15, 16].

In the field of plasmonics, strong coupling has been extensively investigated through the integration of metallic nanoparticles with organic and inorganic materials sustaining excitonic transitions [6]. Under proper conditions, J-aggregating molecules [17–19], dyes [20], quantum dots [21], or two-dimensional materials [22, 23] placed nearby resonant metallic nanoparticles or nanoparticle arrays, have been shown to give rise to strong plasmon-exciton coupling. More importantly, many interesting effects have been predicted and observed in these systems, including coherent emission [17], lasing in nanoparticle arrays [24–26], ultrafast Rabi oscillations [27], chemical dynamics tuning [28], coupling with dark excitonic states [29], and few- to single-emitter coupling [30, 31]. However, high absorption losses in metallic materials still remain the main drawback of studying strong coupling effects in plasmonics, given the resulting broad resonances with extremely short lifetimes, of the order of a few femtoseconds. Moreover, plasmonic materials suffer from heating effects that can hinder the access to nonlinearities, and from a poor integration with existing device technology [32]. In this context, the pursuit of alternative platforms for studying light-matter interactions at the nanoscale becomes particularly important.

From this point of view, high-refractive-index dielectrics have recently been considered as a possible alternative for generating localized optical resonances at the nanometer length scale [33]. In this case, rather than from collective oscillations of free charge carriers, optical resonances arise as a result of the oscillation of polarization charges and the circular displacement current inside the particles when the light wavelength and the particle size become comparable [34]. Even though this behavior is well known since Mie's works on scattering by small particles [35], it is now raising new interest because of the unique possibilities offered in terms of the excitation of magnetic dipolar and multipolar resonances, the control of the light scattering pattern [36, 37], and the presence of anapole resonances [38]. The optical properties of these particles have been investigated for applications in sensing [39], metasurfaces [40], local field enhancement and nonlinearities [41]. Furthermore, strong light-matter coupling has been predicted and investigated in these systems when interacting with excitons, and it was recently shown in two-dimensional transition-metal-dichalcogenide nanodisks (NDs), simultaneously hosting the excitonic and the Mie resonances [42]. By contrast, high-refractive-index nanospheres have been theoretically studied showing the accessibility of the strong coupling regime with dyes having sufficient oscillator strength [43], while experiments in a similar system have shown a peak splitting, though appearing well below the strong coupling criterion [44], and thus being only an induced-transparency effect [45]. Moderate-refractive-index nanoparticles have been investigated as well, showing a weak-coupling behavior [46].

Here we report on the appearance of peak splitting of Mie resonances of silicon NDs interacting with a molecular J-aggregate. Unlike nanospheres, lower-symmetry geometries enable the magnetic dipole (MD) and electric dipole (ED) resonances to be independently tuned [47]. Exploiting this, we investigated the light-matter coupling behavior of the two separately, finding the MD to be in the strong coupling regime and the ED of larger NDs resonating at the same frequency to be at the threshold between an induced transparency effect and the strong coupling. This behavior can be understood in terms of the different near-field profiles of the two resonances, resulting in a different overlap with the surrounding excitonic layer.

2 Results and discussion

The dielectric system of interest in the present work is composed of individual silicon NDs. The cylindrical geometry, as we will show in the following, was chosen because of the straightforward fabrication procedure, and the possibility to independently tune the MD and ED resonances by geometric considerations [47, 48], a possibility that is not offered in the more symmetric case of nanospheres [49].

Before introducing and discussing the experimentally observed properties of those structures, we performed numerical calculations to predict their optical behavior, as shown in Figure 1. In Figure 1A, the numerically calculated scattering spectrum is reported in color scale for silicon NDs with 100 nm thickness and diameters ranging from 100 nm to 300 nm. The spectra have been calculated for an isolated ND in air, with the aid of the extended boundary-condition method (EBCM) for the evaluation of the scattering T-matrix of non-spherical particles (see Section 4 for details) [50]. Here, small diameter NDs show an intense sharp resonance at short wavelengths, superlinearly redshifting with increasing ND diameter. As the ND diameter increases, lower intensity higher-order resonances appear at shorter wavelengths, with an almost linear dispersion as a function of the ND diameter. This behavior, which is well-known in high-refractive-index NDs [51], can be exploited to achieve highly directional scattering when engineering resonant magnetic and electric resonances [36, 37].

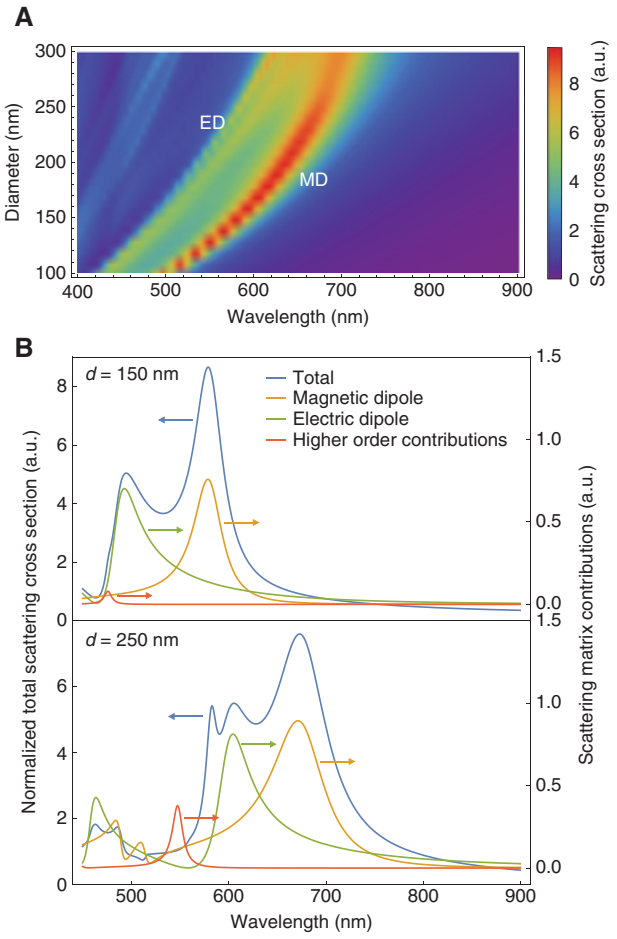

Figure 1: Calculated individual nanodisk scattering.
(A) Calculated scattering spectra in color scale, for silicon nanodisks with 100 nm thickness and diameter ranging from 100 nm to 300 nm. The visible Mie resonances show a continuous redshift with increasing nanoparticle size, while higher-order contributions appear for larger particles. (B) Calculated resonance decomposition for small- (150 nm, top) and large-diameter (250 nm, bottom) nanodisks. The lowest energy resonance in both cases has a magnetic dipole character (orange line). The second peak, appearing at higher energy for larger particles, has instead an electric dipole character (green line), while multipolar contributions (red line) also appear at even shorter wavelengths. The arrows indicate to which y axis (left or right) corresponds each curve.

Although the absence of a substrate is an oversimplification of any practical system, the physical picture offered by the EBCM is powerful in providing a straightforward way to characterize the nature of the resonances observed in the scattering spectrum. In fact, since the EBCM is based on expanding the incident and scattered fields in spherical waves, the method enables identification of the resonances in terms of angular-momentum indices, thus assigning a predominant electric (magnetic) dipole, quadrupole etc. character to them (see Section 4). When we analyze the modes in Figure 1, what we show is not the contribution of any specific element to the scattering cross section, as is usually done in the case of spherical nanoparticles [49], but rather the (renormalized) magnitude of the relevant matrix element. In the case of spherical particles, the method reduces to the well-known Mie theory [35]. Equivalent analysis can be performed in terms of multipole decomposition [52].

The results of the scattering matrix contributions are shown in Figure 1B (right-hand axis), together with the total scattering cross section (left-hand axis). Here, the long wavelength peak appearing in small-diameter NDs ($d = 150$ nm) can be ascribed to an MD resonance. By contrast, a second scattering peak appears at shorter wavelengths, with predominant ED character (green solid line in Figure 1B), and higher order multipoles appear at even shorter wavelengths for larger ($d = 250$ nm) NDs. According to Mie theory for spherical nanoparticles, the MD resonance arises when the effective wavelength of light inside the particle (λ/n, with n being the refractive index of the particle) equals its diameter d. This is also the case here for the smallest ND (see Figure 1A), the diameter and height of which are both 100 nm, and it is reasonable to approximate the particle shape by that of a sphere. In fact, considering that the refractive index of silicon in the ultraviolet spectral range is approximately $n \sim 4.5$ [53], the MD resonance is expected to resonate at $\lambda = 450$ nm and the observed peak is centered at $\lambda = 490$ nm.

Silicon NDs with the same geometrical parameters as those numerically investigated were fabricated on a sapphire substrate. Sapphire has a slightly higher refractive index ($n = 1.775$ at $\lambda = 500$ nm) than other commonly used substrates like quartz or glass, and it was chosen because

of the availability of commercial high-quality silicon-on-sapphire wafers. The presence of a moderate refractive index substrate has been shown to result in an increase of the radiative damping and a slight broadening of the MD and ED resonances of the supported dielectric particles, together with a decrease in the intensity of the scattering peaks, especially when a large contact area exists between nanoparticles and substrate, mainly because of the displacement current loop extending into the substrate [47].

The nanofabrication approach is sketched in Figure 2A. A silicon-on-sapphire substrate with a 100 ± 10 nm thick silicon layer was spin coated with a 200 nm thick hydrogen silsesquioxane, used as a negative-tone resist for electron-beam lithography. NDs with different diameters (ranging from 100 nm to 300 nm) were fabricated, arranged in 15×15 square lattices with 3 μm pitch, so as to minimize near-field interactions between neighboring particles and enable single-particle measurements, with negligible diffractive effects in the visible spectral range given the large lattice constant and the limited number of particles [54]. The sample was then plasma etched, followed by buffered HF (BHF) wet etching to remove any remaining exposed resist (see Section 4 for the details). Scanning electron microscope and optical dark-field microscope images of the resulting final sample are shown in Figure 2B.

The sample was optically investigated by dark-field spectroscopy on an inverted optical microscope. Broadband light from a tungsten lamp was focused at a grazing angle of $\theta \sim 78°$ by a 100×, 0.95 numerical aperture objective lens, used also to collect the back-scattered light. The real image of the sample was then reconstructed on the entrance slit of an imaging spectrometer equipped with a charge-coupled device camera. In this way, the proper in-plane alignment of the sample enables the simultaneous measurement of all the aligned 15 nanoparticles in a lattice column (see Supporting Information).

The measured ND back-scattering spectra in the investigated diameter range are shown in Figure 2C. Similarly to the calculated results in Figure 1A, bright optical resonances appear as scattering peaks, spanning the whole visible to near-infrared spectral range, and redshifting with increasing ND diameter. In particular, small diameter NDs are characterized by an individual sharp resonance at short wavelengths, resulting in bright colors when observed under dark-field excitation (Figure 2B) and corresponding to the MD resonance observed in Figure 1B. As the ND diameter exceeds 150 nm, the MD resonance becomes weaker, while higher-order resonances (ED and multipoles) of comparable strength appear at shorter wavelengths, continuously redshifting as the ND diameter increases. While the resonance dispersion as a function of the particle diameter and the peak position resembles the calculated behavior, the relative intensity of the scattering peaks and their absolute energy position deviates from the map in Figure 1A, mainly as a result of deviations from the nominal ND dimensions and of the presence of a moderate refractive index substrate [47] in the experiments.

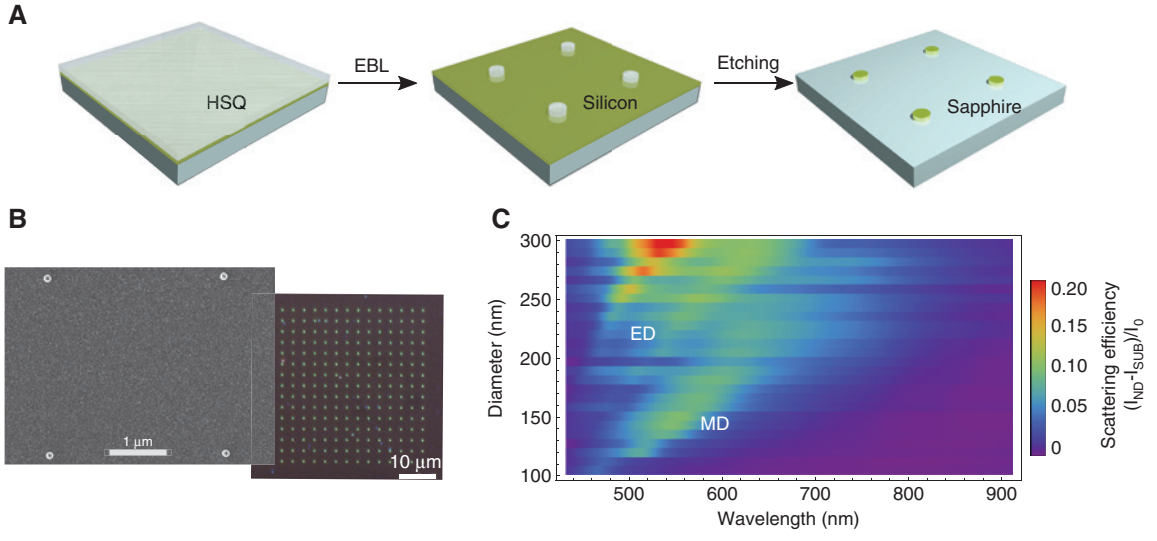

Figure 2: Nanofabrication and optical characterization of silicon nanodisks.
(A) Sketch of the nanofabrication procedure. Hydrogen silsesquioxane (HSQ) was used as an electron-beam resist for electron-beam lithography (EBL) on a silicon-on-sapphire substrate, followed by plasma etching of silicon and wet etching of the exposed resist. (B) Scanning electron micrograph and dark-field optical image of typical fabricated structures arranged in a 3 μm pitch, with 110 nm and 150 nm diameter nanodisks, respectively. (C) Measured back-scattering spectra in color scale as a function of the nanodisks diameter.

In order to investigate light-matter interactions supported by silicon NDs, an organic J-aggregating cyanine dye (5,6-dichloro-1-ethyl-3-sulfobutyl-2-(3-(5,6-dichloro-1-ethyl-3-sulfobutyl benzimidazolinylidene-1-propenyl) benzimidazolium hydroxide, inner salt, sodium salt or TDBC) was drop-casted from a dilute methanol solution on the sample (see Section 4 for the details). This particular dye was chosen because of its high-energy J-aggregate absorption band centered at 585 nm (shown in Figure 3A), where the MD and ED resonances of the silicon NDs are sharp and well separated in energy (see Figure 1A), so as to enable the investigation of the coupling behavior of the two resonances separately. The sample was then studied by dark-field back-scattering spectroscopy, the results of which are shown in Figure 3B–E and compared to numerical results (see Section 4 for details). For small diameter NDs, the MD resonance of which is highly detuned with respect to the J-aggregate exciton energy (Figure 3B), the scattering spectrum is characterized by an intense peak at the MD resonance, the energy position of which is unaltered with respect to the case without molecules. A lower-intensity asymmetric peak also appears around the exciton energy, which can be ascribed to photoluminescence from the J-aggregated dye, shown as a black line in Figure 3A (see Section 4 for details). By contrast, when the MD is resonant at the exciton energy (Figure 3C and D) a peak splitting arises, while the ED peak at high energy remains unchanged. The same behavior is observed as the diameter of the NDs is further increased (Figure 3E): here the ED is tuned in resonance with the exciton energy, while the MD appears as a broad peak at longer wavelengths, with the same energy as the bare ND and increased intensity due to the high refractive index molecular superstrate [47]. This behavior suggests that, in our geometry, no significant cross-talk takes place between the MD and the ED, and that the two resonances couple with the exciton mode without affecting each other. This particular condition can be, in principle, tuned by changing the NDs aspect ratio, thus modifying the ED-MD detuning. In this case, in fact, a dye-mediated interaction between the two resonances could arise, resulting in a three-coupled oscillators system, where all the resonances are simultaneously affected by the near-field coupling. We note here that, although a further increase of the ND diameter would also result in the resonant tuning of higher order resonances at the exciton energy, in this case, the presence of several contributions centered at similar energy would not enable a clear analysis of the coupling (see Supporting Information).

To verify the nature of the Mie-exciton light-matter coupling for the MD and the ED, we extracted the peaks' energy positions for all the fabricated diameters, as shown in Figure 4 as a function of each resonance (i.e. either MD or ED) detuning δ with respect to the exciton energy. Here, an anti-crossing behavior arises when both the MD and ED cross the exciton energy ($E_{exc} = \hbar\omega_{exc} = 2.11$ eV). Considering that the MD and ED are mutually non-interacting,

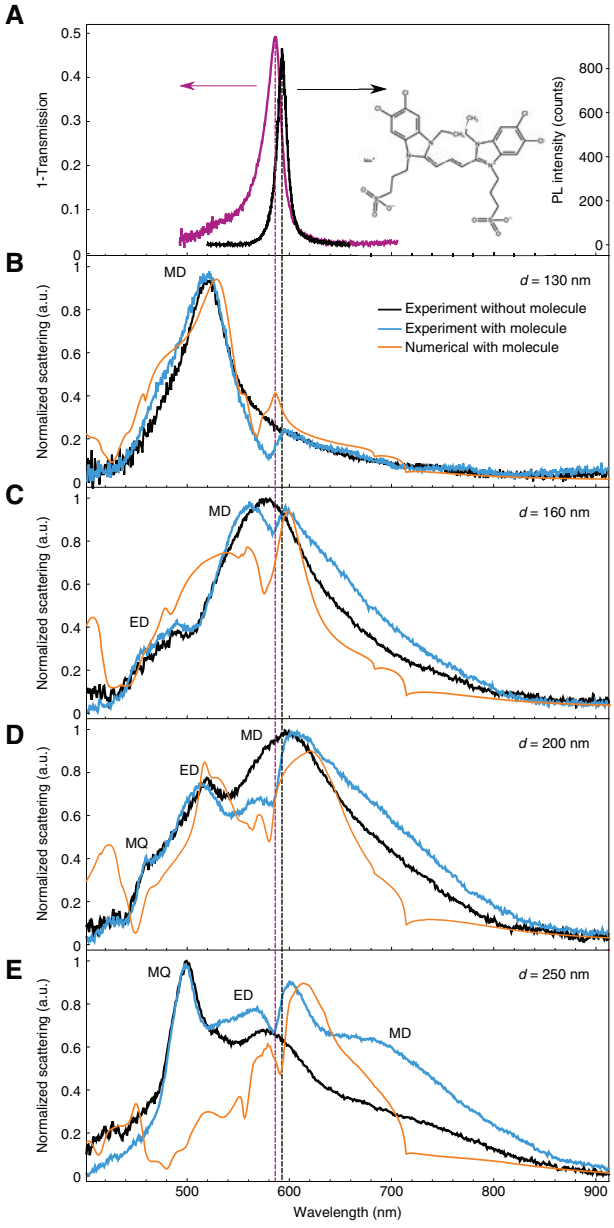

Figure 3: Resonance splitting in the scattering spectra. (A) Absorption (red) and photoluminescence (black) spectra of the J-aggregated dye (TDBC), the chemical structure of which is shown in the inset. (B–E) Evolution of the Mie-exciton coupling as a function of the nanodisk diameter. The black curves correspond to the nanodisk spectra without molecules, while the blue curves are the corresponding spectra in the presence of the dye. The orange spectra are numerically calculated for a silicon nanodisk with a thin (20 nm) dye layer on top (see Section 4).

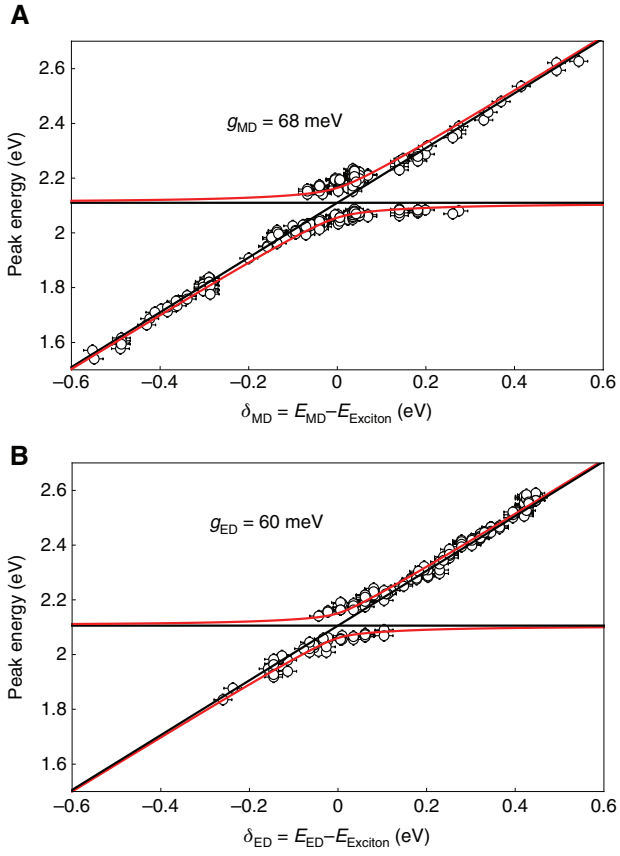

Figure 4: Magnetic and electric dipole resonance anticrossing. Anti-crossing behavior of the observed peak splitting as a function of the bare Mie-exciton detuning for the magnetic dipole (A) and the electric dipole (B) resonances. Red lines show the fitting based on a two coupled oscillators model, with only the coupling strength g as a fitting parameter. The fitting result is indicated in the inset.

each resonance dispersion can be fitted independently with a standard two-coupled-oscillators model:

$$\begin{pmatrix} \omega_1 - i\frac{\gamma_1}{2} & g \\ g & \omega_2 - i\frac{\gamma_2}{2} \end{pmatrix} \begin{pmatrix} a_1 \\ a_2 \end{pmatrix} = \omega \begin{pmatrix} a_1 \\ a_2 \end{pmatrix} \tag{1}$$

where ω_j ($j=1, 2$) are the frequencies of the uncoupled initial states a_j, and g is the coupling strength between the selected Mie resonance ($j=1$) and the excitonic transition of the dye ($j=2$). In our case, $\hbar\gamma_2 = \hbar\gamma_{exc} = 40$ meV, while $\hbar\gamma_1 = \hbar\gamma_{MD} \simeq 120$ meV for the MD and $\hbar\gamma_1 = \hbar\gamma_{ED} \simeq 150$ meV for the ED resonances, as obtained by fitting the numerical scattering spectra (see Supporting Information). We can thus fit the experimental data with only the coupling constant as a fitting parameter, resulting in a coupling strength $\hbar g_{MD} = 68 \pm 2$ meV for the MD resonance and $\hbar g_{ED} = 60 \pm 3$ meV for the ED resonance. A similar result was found by numerical calculations on the coupled system (see Section 4 for details), obtaining $\hbar g_{MD} = 72 \pm 2$ meV and $\hbar g_{MD} = 59 \pm 2$ meV.

The condition to formally evaluate if one system is in the strong coupling regime has been recently discussed in the literature [6, 55]. Briefly, the solution of the two-coupled-oscillators problem at zero detuning ($\omega_2 = \omega_1 = \omega_0$) reads:

$$\omega_\pm = \omega_0 - i\frac{\gamma_1}{4} - i\frac{\gamma_2}{4} \pm \frac{1}{4}\sqrt{(4g)^2 - (\gamma_1 - \gamma_2)^2}, \tag{2}$$

where $\omega_\pm$ are the energies of the resulting hybrid states. It may then seem that a condition for defining the onset of the strong coupling could rely on the maximization of the splitting through the term in the square root, that is $2g > |\gamma_1 - \gamma_2|/2$. However, as we will explain in the following, in the presence of significant damping this condition can be interpreted as only necessary but not sufficient.

To ease our discussions, we define the following quantities: $2\omega_{12} \equiv \sqrt{(4g)^2 - (\gamma_1 - \gamma_2)^2}$ and $Q_{12} \equiv 2\omega_{12}/(\gamma_1 + \gamma_2)$. Next, solving for the dynamics of an initially excited emitter and an empty cavity, one can obtain exact analytical expressions for the occupation factors for the emitter and the cavity, i.e. $|a_1(t)|^2$ and $|a_2(t)|^2$. Whereas the literature offers several more or less appealing figures of merit, the point here is that the above parameterizations constitute the one and only natural re-scaling of the time variable in the context of the analytically exact solution to the dynamics (see Supporting Information). In the large-g limit, the solutions are obtained straightforwardly, reading:

$$\begin{Bmatrix} |a_1(t)|^2 \\ |a_2(t)|^2 \end{Bmatrix} \simeq \exp\left(-\frac{\omega_{12} t}{Q_{12}}\right) \times \begin{Bmatrix} \sin^2\left(\frac{1}{2}\omega_{12} t\right) \\ \cos^2\left(\frac{1}{2}\omega_{12} t\right) \end{Bmatrix}. \tag{3}$$

Thus, ω_{12} is indeed the characteristic Rabi-like frequency of the oscillations, while in the spirit of cavity ring-down-spectroscopy, Q_{12} is a quality factor that quantifies the number of oscillations of the system, before the overall occupation decays in the presence of damping, i.e. $|a_1(t)|^2 + |a_2(t)|^2 \simeq \exp\left(-\frac{\omega_{12} t}{Q_{12}}\right)$. Similar figures of merit expressed in a slightly different notation have appeared elsewhere [56]. As such, $Q_{12} = 1$ unambiguously marks the transition from weak to strong coupling. In other words, strong coupling implies that $2g > 2g^* \equiv \sqrt{\frac{\gamma_1^2 + \gamma_2^2}{2}}$. This inequality, in the limit of $\gamma_1 \sim \gamma_2$ becomes $2g \gtrsim \frac{\gamma_1 + \gamma_2}{2}$, a condition that was shown to coincide with the coupled-system spectrum becoming flat-topped [55]. Both of these inequalities are usually used in the literature for defining

the threshold for the strong coupling regime. In our case, we get $2\hbar g^*_{MD} \sim 90$ meV and $2\hbar g^*_{ED} \sim 110$ meV, thus demonstrating that both the MD and the ED can enter the strong coupling regime. We underline here that the linewidth estimation is based on the fitting of the numerical spectra shown in Figure 1B, that is the only way to access the individual resonance contribution, without possible inhomogeneous broadening mechanisms arising from sample inhomogeneities at the single particle level. In fact, the full fitting of experimental spectra usually requires several Lorentzian contributions to be taken into account, which makes the fitting itself and the evaluation of a physically meaningful linewidth difficult to interpret. However, we emphasize that since the peak splitting behavior, as we will show in the following, is well reproduced by numerical calculations with both the extended layer multiple scattering (ELMS) [57] and the discontinuous Galerkin time-domain (DGTD) method [58, 59] (see Section 4), it is reasonable to assume the numerical linewidth as a reference for the strong coupling threshold estimation.

A further important feature of the strong light-matter interaction regime in nanoparticle-based systems is the observation of a peak splitting also in the absorption or extinction cross section of the hybrid system, since it has been shown that a peak splitting and an anti-crossing can arise in the scattering spectra even far from the strong coupling, as a consequence of surface-enhanced absorption or induced transparency [60]. Here, while our experimental setup makes measuring absorption harder, numerical simulations performed by DGTD show that similar splittings are indeed observed in absorption (see Figure S4 in Supporting Information), thus conforming to another strong-coupling requirement [45, 60]. Particularly interesting is the case of the exciton-resonant ED (Figure S5B). Here, a peak splitting is observed in absorption but not in the scattering spectrum, where the low energy branch visibility is lowered by the presence of the detuned MD at lower energies. This behavior can be expected from the measured coupling $2\hbar g_{ED} = 120 \pm 6$ meV, which is of the same order of magnitude as the predicted strong coupling limit $2\hbar g^*_{ED} = 110$ meV, thus putting this resonance at the threshold between the strong coupling and an induced transparency effect.

The observed splittings are nevertheless of the same order of magnitude as those predicted for silicon nanospheres in a core-shell geometry [43, 61], and as the ones reported for plasmonic systems on individual and arrays of particles interacting with the same molecule [18, 19], thus confirming that high-refractive-index nanoparticles can be a valid alternative platform to metals, for strong coupling applications.

Another key effect observed in our system is the difference in the coupling strength between the MD and the ED resonances, observed both experimentally and numerically. Contrary to what one might perhaps presume, the MD shows a larger coupling strength compared to the ED. In general, since the electromagnetic field profiles are expected to be spatially different for the two resonances, there is every reason to expect the frequency splittings to differ as well. This is because the light-matter coupling constant g can be considered as an indirect measure of the overlap between the electric field of one optical resonance and the excitons localized in the dye layer deposited in the near-field of the nanoparticle.

In order to check this, we performed numerical calculations on a bare silicon ND geometry excited at normal incidence with a plane wave, and calculated the electromagnetic field total intensity (color scale) and the electric field amplitude (arrows) at resonance ($\lambda = 590$ nm), in a vertical plane cutting the silicon ND in its centre, as shown in Figure 5 (see Section 4 for details). We chose the two ND diameters corresponding to the zero detuning condition for the MD ($d = 150$ nm, Figure 5A) and the ED ($d = 230$ nm, Figure 5B); for a short discussion on the differences in sizes between experiments and simulations, see Section 4. The results clearly show that the intensity and electric field profiles are completely different in the two cases. For the small ND, the electromagnetic field profile at resonance resembles that of an MD, with a clear circulating electric field loop inside the particle, partially extending into the substrate. By contrast, the larger ND shows an ED behavior, with an antinode in the electric field amplitude at the particle center. It is also clear that the electric field intensity is higher all around the smaller ND ($d = 150$ nm, Figure 5A), and particularly at the ND sides. Although the numerical results in Figure 3 considered an ordered model with a coaxial thin dye disk lying only on the top surface of the NDs, the real J-aggregate geometrical distribution around the ND is not well-known, and in general, it is natural to expect that a higher field intensity leads to stronger near-field mediated interactions. Furthermore, considering the surface-to-volume ratio as a very rough indication of the ratio between the total electric field energy and the physical space available for the molecules, it is plausible that the smaller ND exhibits a larger splitting. However, given the uncertainty about the positions of the molecules and their dipole orientation distribution, nothing more conclusive than this can be safely stated, and we stress here that particular attention must be paid when studying dielectric systems with overlapping electric and magnetic dipolar resonances. By contrast, fewer degrees of freedom can be offered by two-dimensional materials, the homogeneity

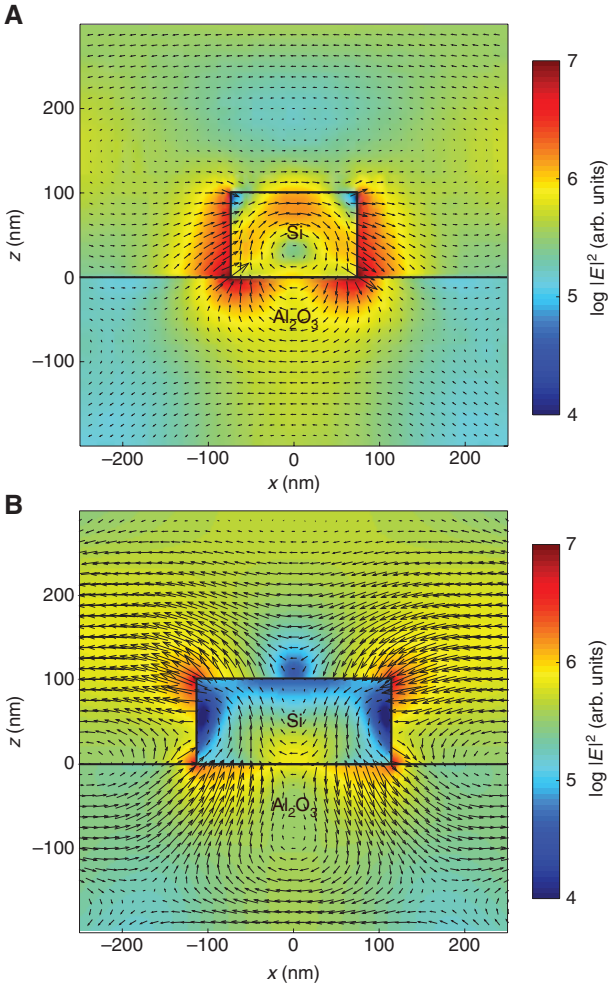

Figure 5: Magnetic and electric dipole near-field profiles. Logarithm of total electric field intensity (color scale) and orientation of the real in-plane part of the electric field (arrows) at resonance and under normal incidence, calculated for silicon nanodisks with (A) 150 nm and (B) 230 nm diameter. Here $z < 0$ represents the sapphire substrate. The smaller disk clearly exhibits a magnetic-dipole-like behavior, with a loop in the electric field amplitude inside the particle, while the larger disk shows an electric dipole behavior, with an antinode at the nanodisk center.

and in-plane dipole orientation of which might result in a simpler system to be studied [43, 61].

3 Conclusions

In summary, we have investigated experimentally and theoretically the light-matter interactions between Mie resonances supported by high-refractive-index silicon NDs and excitons in a J-aggregated dye. The lower geometrical symmetry of our nanoparticles, compared to the nanosphere case, enables spectral separation of the MD and ED resonances, and independent investigation into their coupling with the excitonic dipoles. A significant peak splitting was observed in both cases. In the MD case, the splitting was found to be larger than the losses in the system, thus setting our system in the strong coupling regime. On the contrary, the ED splitting was of the same order of magnitude as the losses, thus suggesting the interaction regime to be at the boundary between the strong coupling and an induced transparency effect. We found that the two different light-matter interaction regimes arise as a consequence of the different near-field profiles of the two resonances, when tuned by geometrical means at the exciton energy. The coupling strength measured in our system is comparable to those reported for similar plasmonic systems, thus confirming that high-refractive-index nanoparticles can be a valid alternative platform to plasmonics for room-temperature strong coupling applications. Moreover, in passing we note that other less lossy high-refractive-index materials may be considered in the future in order to excite even sharper resonances, which can in principle result in a more efficient light-matter coupling and larger splittings. By contrast, realizing strong light-matter interactions on dielectric nanoparticle systems can be interesting when exploiting the salient features of Mie resonances, such as directional scattering and high intrinsic nonlinearities.

4 Methods

4.1 Sample fabrication

A commercial silicon-on-sapphire substrate (University Wafer, Inc., South Boston, MA, USA) was cleaned in acetone and 2-propanol in an ultrasonic bath for 30 min, and then dried with a nitrogen steam. Hydrogen silsesquioxane (Dow Corning Corporation, Midland, MI, USA, XR-1541-006 e-beam resist) was then spin coated on the sample at 500 rpm for 5 s followed by 1200 rpm for 45 s, and then baked on an hot plate at 170°C for 2 min, resulting in a final resist thickness of approximately 200 nm. The nanostructures were written by electron beam lithography with design diameters ranging from 100 nm to 300 nm, in 20 nm steps, and at different doses, so as to obtain a fine diameter tuning. After developing the hydrogen silsesquioxane in tetramethylammonium hydroxide, the silicon beneath was etched. The etching process is a standard BOSCH process, where after an isotropic etch, a passivation process follows. This sequence is repeated until the desired etch depth is achieved. In our case, since one cycle etches approximately 40 nm, we etched the sample for three cycles, ensuring a

complete etch of the silicon layer, as clearly evidenced by the change in the substrate appearance from a semi-opaque green color to completely transparent. Thereafter, a quick 5 min BHF bath removed the hydrogen silsesquioxane layer. The sample was finally cleaned in acetone and 2-propanol. We observe that the electron beam lithography process changes the surface properties of the substrate in the area around the structures, thus making impossible the dye deposition by spin coating without employing surface chemistry. We thus drop-casted the dye (FEW Chemicals GmbH, Bitterfeld-Wolfen, Germany, CAS NO 18462-64-1) from a dilute solution depositing a 2 µl drop on the nanostructured area and slowly drying it with a gentle nitrogen flow. The solution was prepared dissolving the dye in methanol with a 0.1 mM concentration (0.76 mg dissolved in 10 ml). Then 1 ml of this solution was added to 6 ml deionized water. The NDs' diameter was carefully characterized at the end of all the optical measurements by scanning electron beam microscopy. To this aim, the dye was removed by immersing the sample in deionized water, and a 13 nm thick aluminum layer was evaporated onto the whole sample by thermal evaporation to ensure sufficient in-plane conductivity. All the particle arrays optically investigated were then imaged at a 30 keV acceleration voltage.

4.2 Optical characterization

Optical characterization was performed on an inverted optical microscope in dark-field configuration, exciting the sample and collecting back-scattered light through a high numerical aperture (100×, NA = 0.95) objective lens. The optical image of the sample at the output port of the microscope was collected with a 150 mm focal length doublet lens and reconstructed on the entrance slit of an imaging spectrometer with a 200 mm focal length doublet lens. The ND array was carefully aligned with the entrance slit of the spectrometer so as to simultaneously measure 15 particles in a single charge-coupled device image. Unwanted signals from defects on the sample surface were manually removed when analyzing the data. Photoluminescence spectra from the molecular layer were measured on a Raman microscope, exciting with a diffraction-limited spot at $\lambda = 535$ nm. Low power was used for the excitation, so as to avoid photo-bleaching of the dye.

4.3 Numerical calculations

The scattering properties of individual NDs were calculated with an efficient *T*-matrix method [62], namely EBCM [50], the principal characteristic of which is that it takes the boundary conditions of continuity of the tangential components of the fields into account through appropriate surface integrals. The incident field is expanded into vector spherical waves about the origin, with expansion coefficients $a^0_{P\ell m}$, where $P = E, H$ is the polarization, of electric or magnetic type, and ℓ, m are the usual angular momentum indices. Accordingly, the scattered wave is expanded into vector spherical waves with expansion coefficients $a^+_{P\ell m}$, which are connected to those of the incident field through the elements of the *T*-matrix, with:

$$a^+_{P\ell m} = \sum_{P'\ell'm'} T_{P\ell m;P'\ell'm'} a^0_{P'\ell'm'}. \tag{4}$$

For spherical particles, T is diagonal with respect to P and ℓ, and independent of m. For non-spherical particles, however, this no longer holds and, strictly speaking, an unambiguous classification of its eigenvalues in terms of polarization and angular momentum cannot be made. Nevertheless, for relatively small NDs, one largely predominant matrix element always exists, and this is what we plot in Figure 1C. For increasing ND size, the contribution and mixing of off-diagonal elements becomes ever more important, and assigning a predominant character to the resonances – especially higher-order ones – becomes practically impossible. This is strikingly visible in the lower panel of Figure 1C, where the scattering peak at 580 nm cannot be reproduced by any scattering matrix element alone, even though its near-field profile implies that it is predominantly a magnetic quadrupole, while the corresponding *T*-matrix element (red line) peaks at 550 nm, not exactly corresponding to a scattering resonance. Scattering and extinction-cross sections are calculated through:

$$\sigma_{sc} = \frac{1}{q^2} \sum_{P\ell m} \left| \sum_{P'\ell'm'} T_{P\ell m;\,P'\ell'm'} \mathbf{A}^0_{P'\ell'm'} \cdot \hat{\mathbf{p}} \right|^2, \tag{5}$$

$$\sigma_{ext} = -\frac{1}{q^2} \mathrm{Re} \sum_{P\ell m} (\mathbf{A}^0_{P\ell m} \cdot \hat{\mathbf{p}})^* \sum_{P'\ell'm'} T_{P\ell m;P'\ell'm'} \mathbf{A}^0_{P'\ell'm'} \cdot \hat{\mathbf{p}}, \tag{6}$$

where $q = \frac{\omega}{c}\sqrt{\varepsilon\mu}$ is the wavenumber of the incident wave of angular frequency ω in a homogeneous environment with permittivity ε and permeability μ, and c is the velocity of light in vacuum. The matrix elements $\mathbf{A}$ are related to the expansion coefficients $a^0_{P\ell m}$ of an incident plane wave with electric field $\mathbf{E}_0$ and polarization $\hat{\mathbf{p}}$ through [57]:

$$a^0_{P\ell m} = \mathbf{A}^0_{P\ell m}(\mathbf{q}) \cdot \hat{\mathbf{p}} E_0(\mathbf{q}). \tag{7}$$

To describe the J-aggregate/silicon ND system, we use the ELMS method [57], which is ideal for periodic arrays of

spherical or cylindrical scatterers. Initially developed for scatterers with spherical symmetry described through Mie theory [63], the method has been extended through implementation of EBCM, and can efficiently describe transmission and reflection from combinations of stacked arrays of disks or cylinders of various sizes, with the restriction that all arrays have the same two-dimensional periodicity [64–66]. In our case, we consider "birthday cakes" where the role of the cake is played by the silicon ND, and an "icing" of thickness 20 nm and the same diameter is introduced as the molecule. These two-component particles are arranged in square arrays with a lattice constant 720 nm, which ensures that interactions between individual building blocks are minimal, while lattice resonances from the Rayleigh-Wood anomalies are kept outside the wavelength window of interest, as much as possible. Weak interactions for the larger NDs, and small differences between the modeled and real permittivities, explain why slightly smaller particles are required to match the theoretical and experimental spectra, e.g. a diameter of 230 nm is used in the simulations for the 250 nm ND of the last panel of Figure 3. The arrays are illuminated by p-polarized light, incident at an angle of 70°, and reflectance spectra are calculated by integrating the energy flow above the structure over the first Brillouin zone. The coupling strengths are then obtained through the width of the anti-crossing in the reflection spectra at zero detuning. The composite arrays are deposited on a semi-infinite sapphire substrate, described by a relative permittivity equal to 3.13. For the permittivity of silicon we use the experimental values of Green [67], while for the molecule we use a Lorentzian permittivity:

$$\varepsilon_{\mathrm{mol}} = \varepsilon_{\infty} - \frac{f\omega_{\mathrm{exc}}^2}{\omega^2 - \omega_{\mathrm{exc}}^2 + \mathrm{i}\omega\gamma_{\mathrm{exc}}^2}, \tag{8}$$

with $\varepsilon_{\infty} = 2.56$, $\hbar\omega_{\mathrm{exc}} = 2.11$ eV, $\hbar\gamma_{\mathrm{exc}} = 0.33$ eV, and $f = 0.35$.

In all EBCM calculations, we truncate the angular-momentum expansions at $\ell_{\mathrm{max}} = 12$. A larger number of matrix elements corresponding to $\ell_{\mathrm{cut}} = 16$ is required at some steps within the method, although they are not involved in the final calculation of cross sections. Integrals at the surface of the particles are calculated with a Gaussian quadrature integration formula, with 4000–6000 integration points, depending on the ND size. The only additional convergence parameter involved in ELMS is the number of reciprocal-lattice vectors involved in plane-wave expansions, and here 161 vectors were required to achieve convergence.

The field plots in Figure 5 were calculated using the DGTD method [58, 59] using third order polynomials on a tetrahedral mesh with element sizes of 20 nm in the silicon disk, 60 nm in substrate and air close to the disk, and 120 nm elsewhere. Silicon was modeled using a single-pole Lorentz model in order to reproduce the experimental data [67], with a relative error of 2% for wavelengths between 2500 nm and 400 nm. The substrate was modeled with a constant permittivity $\varepsilon_{\mathrm{Al_2O_3}} = 3.133$.

5 Supplemental material

The following files are available free of charge.

- Imaging spectral measurements
- Photoluminescence maps
- High concentration drop casting
- Higher order resonances
- Numerical absorption spectra
- Spectra fitting
- Two-coupled-oscillators model

Acknowledgment: N. A. M. is a VILLUM investigator supported by VILLUM FONDEN (grant No. 16498, Funder Id: http://dx.doi.org/10.13039/100008398). The Center for Nano Optics is financially supported by the University of Southern Denmark (SDU 2020 funding). The Center for Nanostructured Graphene is sponsored by the Danish National Research Foundation (Project No. DNRF103). F.T. is grateful to V. Ratano for resilient and lifelong collaboration. C. T. and C. W. thank Pano Ramix for stimulating discussions. F. T. and C. W. acknowledge funding from MULTIPLY fellowships under the Marie Skłodowska-Curie COFUND Action (grant agreement No. 713694, Funder Id: http://dx.doi.org/10.13039/100011264). Simulations were supported by the DeIC National HPC Centre, SDU.

References

[1] Walls D, Milburn G. Quantum optics. Berlin: Springer, 1994.
[2] Raimond JM, Brune M, Haroche S. Manipulating quantum entanglement with atoms and photons in a cavity. Rev Mod Phys 2001;73:565–82.
[3] Mabuchi H, Doherty AC. Cavity quantum electrodynamics: coherence in context. Science 2002;298:1372–7.
[4] Hümmer T, García-Vidal FJ, Martín-Moreno L, Zueco D. Weak and strong coupling regimes in plasmonic QED. Phys Rev B 2013;87:115419.
[5] Fernández-Domínguez AI, Bozhevolnyi SI, Asger Mortensen N. Plasmon-enhanced generation of nonclassical light. ACS Photonics 2018;5:3447–51.
[6] Törma P, Barnes WL. Strong coupling between surface plasmon polaritons and emitters: a review. Rep Prog Phys 2015;78:013901.

[7] Vesseur EJR, Javier García de Abajo F, Polman A. Broadband Purcell enhancement in plasmonic ring cavities. Phys Rev B 2010;82:165419.
[8] Akselrod GM, Argyropoulos C, Hoang TB, et al. Probing the mechanisms of large Purcell enhancement in plasmonic nanoantennas. Nat Photon 2014;8:835–40.
[9] Jackson JB, Halas NJ. Surface-enhanced Raman scattering on tunable plasmonic nanopar- ticle substrates. Proc Natl Acad Sci U S A 2004;101:17930–5.
[10] Chance RR, Prock A, Silbey R. Molecular fluorescence and energy transfer near interfaces. In: Advances in Chemical Physics, Vol. 37, New York, NY, USA: John Wiley & Sons, 1978:1–65.
[11] Lakowicz JR, Fu Y. Modification of single molecule fluorescence near metallic nanostructures. Laser Phot Rev 2009;3:221–32.
[12] Baffou G, Quidant R. Thermo-plasmonics: using metallic nanostructures as nano-sources of heat. Laser Phot Rev 2013;7:171–87.
[13] Chorsi HT, Lee Y, Alù A, Zhang JXJ. Tunable plasmonic substrates with ultrahigh Q-factor resonances. Sci Rep 2017;7:15985.
[14] Chorsi HT, Zhu Y, Zhang JXJ. Patterned plasmonic surfaces—theory, fabrication, and applications in biosensing. J Microelectromech Syst 2017;26:718–39.
[15] Delteil A, Fink T, Schade A, Höfling S, Schneider C, İmamoğlu A. Towards polariton blockade of confined exciton–polaritons. Nat Mater 2019;18:219–22.
[16] Verger A, Ciuti C, Carusotto I. Polariton quantum blockade in a photonic dot. Phys Rev B 2006;73:193306.
[17] Aberra Guebrou S, Symonds C, Homeyer E, et al. Coherent emission from a disordered organic semiconductor induced by strong coupling with surface plasmons. Phys Rev Lett 2012;108:066401.
[18] Todisco F, D'Agostino S, Esposito M, et al. Exciton–plasmon coupling enhancement via metal oxidation. ACS Nano 2015;9:9691–9.
[19] Zengin G, Johansson G, Johansson P, Antosiewicz TJ, Käll M, Shegai T. Approaching the strong coupling limit in single plasmonic nanorods interacting with J-aggregates. Sci Rep 2013;3:3074.
[20] Todisco F, De Giorgi M, Esposito M, et al. Ultrastrong plasmon–exciton coupling by dynamic molecular aggregation. ACS Photonics 2018;5:143–50.
[21] Gómez DE, Vernon KC, Mulvaney P, Davis TJ. Surface plasmon mediated strong exciton-photon coupling in semiconductor nanocrystals. Nano Lett 2010;10:274–8.
[22] Stührenberg M, Munkhbat B, Baranov DG, et al. Strong light–matter coupling between plasmons in individual gold bi-pyramids and excitons in mono- and multilayer WSe2. Nano Lett 2018;18:5938–45.
[23] Geisler M, Cui X, Wang J, et al. Single-crystalline gold nanodisks on WS2 mono- and multilayers for strong coupling at room temperature. ACS Photonics 2019;6:994–1001.
[24] Ramezani M, Halpin A, Fernández-Domínguez AI, et al. Plasmon-exciton-polariton lasing. Optica 2017;4:31–7.
[25] De Giorgi M, Ramezani M, Todisco F, et al. Interaction and coherence of a plasmon–exciton polariton condensate. ACS Photonics 2018;5:3666–72.
[26] Hakala YK, Moilanen AJ, Väkeväinen AI, et al. Bose–Einstein condensation in a plasmonic lattice. Nat Phys 2018;14:739–44.
[27] Vasa P, Wang W, Pomraenke R, et al. Real-time observation of ultrafast Rabi oscillations between excitons and plasmons in metal nanostructures with J-aggregates. Nat Photonics 2013;7:128–32.
[28] Munkhbat B, Wersäll M, Baranov DG, Antosiewicz TJ, Shegai T. Suppression of photo-oxidation of organic chromophores by strong cou- pling to plasmonic nanoantennas. Sci Adv 2018;4:eaas9552.
[29] Cuartero-González A, Fernández-Domínguez AI. Light-forbidden transitions in plasmon-emitter interactions beyond the weak coupling regime. ACS Photonics 2018;5:3415–20.
[30] Chikkaraddy R, de Nijs B, Benz F, et al. Single-molecule strong coupling at room temperature in plasmonic nanocavities. Nature 2016;535:127–30.
[31] Santhosh K, Bitton O, Chuntonov L, Haran G. Vacuum Rabi splitting in a plasmonic cavity at the single quantum emitter limit. Nat Commun 2016;7:11823.
[32] Naik GV, Shalaev VM, Boltasseva A. Alternative plasmonic materials: beyond gold and silver. Adv Mater 2013;25:3264–94.
[33] Kuznetsov AI, Miroshnichenko AE, Brongersma ML, Kivshar YS, Luk'yanchuk B. Optically resonant dielectric nanostructures. Science 2016;354:aag2472.
[34] Yang Z-J, Jiang R, Zhuo X, Xie Y-M, Wang J, Lin H-Q. Dielectric nanoresonators for light manipulation. Phys Rep 2017;701:1–50.
[35] Bohren CF, Huffman DR. Absorption and scattering of light by small particles. New York: Wiley-Interscience, 1983.
[36] Staude I, Miroshnichenko AE, Decker M, et al. Tailoring directional scattering through magnetic and electric resonances in sub- wavelength silicon nanodisks. ACS Nano 2013;7:7824–32.
[37] Cihan AF, Curto AG, Raza S, Kik PG, Brongersma ML. Silicon Mie resonators for highly directional light emission from monolayer MoS2. Nat Photon 2018;12:284–90.
[38] Yang Y, Zenin VA, Bozhevolnyi SI. Anapole-assisted strong field enhancement in individual all-dielectric nanostructures. ACS Photonics 2018;5:1960–6.
[39] Yavas O, Svedendahl M, Dobosz P, Sanz V, Quidant R. On-a-chip biosensing based on all-dielectric nanoresonators. Nano Lett 2017;17:4421–6.
[40] Yu YF, Zhu AY, Paniagua-Domínguez R, Fu YH, Luk'yanchuk B, Kuznetsov AI. High-transmission dielectric metasurface with 2π phase control at visible wave- lengths. Laser Phot Rev 2015;9:412–8.
[41] Gigli C, Marino G, Suffit S, et al. Polarization- and diffraction-controlled second-harmonic generation from semiconductor metasurfaces. J Opt Soc Am B 2019;36:E55–64.
[42] Verre R, Baranov DG, Munkhbat B, Cuadra J, Käll M, Shegai T. Transition metal dichalcogenide nanodisks as high-index dielectric Mie nanoresonators. Nat Nanotechnol 2019;14:679–83.
[43] Tserkezis C, Gonçalves PAD, Wolff C, Todisco F, Busch K, Mortensen NA. Mie excitons: Understanding strong coupling in dielectric nanoparticles. Phys Rev B 2018;98:155439.
[44] Wang H, Ke Y, Xu N, et al. Resonance coupling in silicon nanosphere–J-aggregate heterostructures. Nano Lett 2016;16:6886–95.
[45] Antosiewicz TJ, Apell SP, Shegai T. Plasmon–exciton interactions in a core–shell geometry: from enhanced absorption to strong coupling. ACS Photonics 2014;1:454–63.
[46] Ruan Q, Li N, Yin H, Cui X, Wang J, Lin H-Q. Coupling between the Mie resonances of Cu2O nanospheres and the excitons of dye aggregates. ACS Photonics 2018;5:3838–48.

[47] van de Groep J, Polman A. Designing dielectric resonators on substrates: Combining magnetic and electric resonances. Opt Express 2013;21:26285–302.
[48] Evlyukhin AB, Reinhardt C, Chichkov BN. Multipole light scattering by non- spherical nanoparticles in the discrete dipole approximation. Phys Rev B 2011;84:235429.
[49] Evlyukhin AB, Novikov SM, Zywietz U, et al. Demonstration of magnetic dipole resonances of dielectric nanospheres in the visible region. Nano Lett 2012;12:3749–55.
[50] Mishchenko MI, Travis LD, Lacis AA. Scattering, absorption, and emission of light by small particles. Cambridge: Cambridge University Press, 2002.
[51] Decker M, Staude J. Resonant dielectric nanostructures: a low-loss platform for functional nanophotonics. J Opt 2016;18:103001.
[52] Butakov N, Schhuller JA. Designing multipolar resonances in dielectric metamaterials. Sci Rep 2016;6:38487.
[53] Aspnes DE, Studna AA. Dielectric functions and optical parameters of Si, Ge, GaP, GaAs, GaSb, InP, InAs, and InSb from 1.5 to 6.0 eV. Phys Rev B 1983;27:985–1009.
[54] Evlyukhin AB, Reinhardt C, Seidel A, Luk'yanchuk BS, Chichkov BN. Optical response features of Si-nanoparticle arrays. Phys Rev B 2010;82:045404.
[55] Khitrova G, Gibbs HM, Kira M, Koch SW, Scherer A. Vacuum Rabi splitting in semiconductors. Nat Phys 2006;2:81–90.
[56] Yang ZJ, Antosiewicz TJ, Shegai T. Role of material loss and mode volume of plasmonic nanocavities for strong plasmon-exciton interactions. Opt Express 2016;24: 20373–81.
[57] Gantzounis G, Stefanou N. Layer-multiple-scattering method for photonic crystals of nonspher- ical particles. Phys Rev B 2006;73:035115.
[58] König M, Busch K, Niegemann J. The discontinuous Galerkin time-domain method for Maxwell's equations with anisotropic materials. Photonics Nanostruct 2010;8:303–9.
[59] Busch K, König M, Niegemann J. Discontinuous Galerkin methods in nanophotonics. Laser Photonics Rev 2011;5:774–809.
[60] Zengin G, Gschneidtner T, Verre R, et al. Evaluating conditions for strong coupling between nanoparticle plasmons and organic dyes using scattering and absorption spectroscopy. J Phys Chem C 2016;120:20588–96.
[61] Lepeshov S, Wang M, Krasnok A, et al. Tunable resonance coupling in single si nanoparticle–monolayer WS2 structures. ACS Appl Mater Interfaces 2018;10:16690–7.
[62] Waterman PC. Matrix formulation of electromagnetic scattering. Proc IEEE 1965;53:805–12.
[63] Stefanou N, Yannopapas V, Modinos A. Heterostructures of photonic crystals: frequency bands and transmission coefficients. Comput Phys Commun 1998;113:49–77.
[64] Tserkezis C, Papanikolaou N, Gantzounis G, Stefanou N. Understanding artificial optical magnetism of periodic metal-dielectric-metal layered structures. Phys Rev B 2008;78:165114
[65] Tserkezis C, Stefanou N. Uniaxial crystals of metallodielectric nanosandwiches: effective optical parameters and negative refraction. J Opt 2010;12:155103.
[66] Tserkezis C, Stefanou N. Calculation of waveguide modes in linear chains of metallic nanorods. J Opt Soc Am B 2011;29:827–32.
[67] Green MA. Self-consistent optical parameters of intrinsic silicon at 300 K including temperature coefficients. Sol Energy Mater Sol Cells 2008;92:1305–10.

Supplementary Material: The online version of this article offers supplementary material (https://doi.org/10.1515/nanoph-2019-0444).